# Electromagnetic wave absorption performance of $Fe_3O_4$/activated carbon-natural resin nanocomposite

Mahsa Mahmoodi[1], Bagher Aslibeiki[1,2,*], Reza Peymanfar[3,4,5], Hamid Naghshara[1],
Rajesh Kumar Rajagopal[2], Yue Zhao[6], Davide Peddis[7,8], Tapati Sarkar[2,*]
( 1. *Faculty of Physics*, *University of Tabriz*, 51666-16471, *Tabriz*, *Iran*;
2. *Division of Solid State Physics*, *Department of Materials Science and Engineering*, *Uppsala University*, *SE*-751 03, *Sweden*;
3. *Department of Chemical Engineering*, *Energy Institute of Higher Education*, 39177-67746, *Saveh*, *Iran*;
4. *Iranian Society of Philosophers*, *Department of Science*, 13187-76511, *Tehran*, *Iran*;
5. *Peykareh Enterprise Development CO.*, 15149-45511, *Tehran*, *Iran*;
6. *College of Materials Science and Technology*, *Nanjing University of Aeronautics and Astronautics*, *Nanjing* 210016, *China*;
7. *Dipartimento di Chimica e Chimica Industriale* & *INSTM*, *nbM2-Lab*, *Università degli Studi di Genova*, *Via Dodecaneso 31*, *I*-16146, *Genoa*, *Italy*;
8. *Institute of Structure of Matter*, *National Research Council*, *nM2-Lab*, *Via Salaria km 29.*300, *Monterotondo Scalo* 00015, *Roma*, *Italy* )

**Abstract**: There has recently been a fundamental need to develop high efficiency microwave absorbers to reduce electro-magnetic pollution. It is often very difficult to obtain superior absorption with only one material, so we have explored composites using fillers of activated carbon derived from biological material (oleaster seeds) and resin (apricot tree gum) with $Fe_3O_4$ in a paraffin wax matrix to improve the dielectric properties and achieve a high specific surface area. A 1 mm thick layer of a $Fe_3O_4$ + resin (FEOR), with the magnetic nanoparticles anchored to the gum, resulted in a reflection loss of −71.09 dB. We compared this with the results for composites using a filler of $Fe_3O_4$ + activated carbon, and one with a three-component filler of $Fe_3O_4$ + activated carbon + resin which had a very porous structure that had a direct effect on the surface polarization. However, the FEOR sample had near-ideal impedance matching, close to 1, which resulted in high absorption performance. In addition, the presence of defects improves microwave attenuation by dipole polarization and charge carrier trapping. This work suggests the use of new types of biomaterials to increase microwave absorption.

**Key words:** Activated carbon; Oleaster seeds; Gum; Magnetite; Microwave absorption

## 1 Introduction

Recent advancements in electronic devices across multiple fields, including communication, military, aerospace, Internet of Things (IoT), and artificial intelligence (AI), have greatly improved our daily lives. However, the abundant presence of electromagnetic radiation from these devices has given rise to a new kind of environmental pollution, posing significant challenges to our ecosystem and human well-being[1]. Therefore, there is a need to develop materials with electromagnetic wave absorbing capacity that can mitigate electromagnetic radiation pollution, and intense research is focused on this field[2–4]. Low-weight materials and green synthesis methods are particularly important both from a functional as well as sustainability point of view[5]. To address the weight issue, mesoporous and microporous structures are preferable, which effectively increase the specific surface area and reduce the weight of the material for equal performance[6,7]. Additionally, they also provide the possibility to incorporate secondary phases into the porous structure that could enhance the functionality through impedance matching of the two phases[8]. For example, in Wu et al.'s work, a biomass hierarchical porous carbon (BHPC) with micropores, mesopores and macropores obtained from rice husk was prepared using potassium KOH activation and one-step carbonization. The BHPC sample exhibited a

---

**Received date:** 2024-06-12; **Revised date:** 2024-09-04

**Corresponding author:** Bagher Aslibeiki. E-mail: b.aslibeiki@tabrizu.ac.ir;
Tapati Sarkar. E-mail: tapati.sarkar@angstrom.uu.se

**Author introduction:** Mahsa Mahmoodi. E-mail: mahmoodi76mahsa@gmail.com

minimum reflection loss ($RL_{min}$) of −47.463 dB at 9.79 GHz, and the effective absorption bandwidth was 81% of the X-band. The synergistic effects of macropores, mesopores and micropores contributed to the adsorption performance of BHPC. The macropores in BHPC form a conductive network to promote the conductivity loss of the material. It showed good absorption performance for electromagnetic waves due to good impedance matching, high dielectric loss capacity, large specific surface area and reasonable pore diameter distribution[9]. Zhao et al. used the inherent microstructure characteristic of biomass in nature as a potential way to deal with the problem of electromagnetic interference. They showed the formation of sufficient porous structure in sudden absorption at low relative pressure and a hysteresis loop at high relative pressure, which elucidated the coexistence of micropores and mesopores in a hierarchically porous magnetic carbon (HPMC). These abundant micro/mesoporous structures create a large number of air-solid interfaces in the sample, which can induce strong surface polarization under an external electromagnetic field. It exhibits excellent electromagnetic wave performance with minimum reflection loss ($RL_{min}$) of −52 dB and a wide effective absorption bandwidth of 5 GHz at a low filler content[10].

Carbonaceous structures derived from biological materials have demonstrated a high conductivity and relaxation loss ability, making them a suitable option for microwave-absorbing structures[11−13]. The porous morphology of a carbon-based material reduces its density, creates microcurrents and multiple reflections, and enhances polarization loss in an absorber, thereby amplifying microwave attenuation[14−16]. The synthesis of carbonaceous structures such as graphene oxide and carbon nano-coil, wires, tubes, and rods is challenging due to the complex synthesis processes involved and high preparation costs. Therefore, highly porous low-cost biomass derived structures using agricultural residues[17], wood[18], animal waste[19], aquatic plants[20], algae[21], human waste[9], industrial waste[22], etc. offer more viable alternatives to enhance the performance of microwave absorbing materials. To increase their efficiency for microwave absorption, biological materials should be pre-treated by various methods before pyrolysis. Single-component carbon-based dielectric materials may have disadvantages like impedance mismatch, which could be circumvented by the use of composites with magnetic materials. Apart from dielectric materials, some metals also show conducive magnetic properties like enhanced magnetic permeability. Metal oxides like ferrite nanocomposites exhibit notable properties such as flexibility and thermal stability[23]. Microwave absorbers require low density for practical applications, so this should be considered when selecting the raw materials. The combination of carbon-based materials with ferrites improves impedance matching through magnetic losses, enhancing microwave absorption[24,25]. Bare $Fe_3O_4$ nanoparticles exhibit a weak reflection loss (RL), usually above −10 dB[26]. However, when $Fe_3O_4$ nanoparticles are dispersed on activated carbon or a resin matrix in a suitable proportion, the fabricated structure is expected to exhibit better impedance matching. In our previous work, compositing activated carbon obtained from oleaster seeds with $Fe_3O_4$ magnetic nanoparticles was used to investigate the electromagnetic wave absorption[27]. The $Fe_3O_4$/activated carbon (AC) composite showed a microwave absorption performance of about RL = −51 dB with a thickness of 1 mm, and 3.66 GHz efficient bandwidth, arising from impedance matching, eddy current loss, natural resonance and reflections[27,28]. In another work by Rusly et al. , $BiFeO_3$ (BFO)/epoxy resin composite structure was found to enhance the absorption efficiency due to the coupled magneto-dielectric properties of BFO. The composite with 70% resin filler showed good performance, with $RL_1$ = −26 dB and $RL_2$ = −40.5 dB at the frequencies of 9.1 and 11.3 GHz, respectively[29].

In this work, spinel iron oxide is utilized to induce high magnetic loss. $Fe_3O_4$ is ferrimagnetic due to the coexistence of ferrous and ferric cations, leading to a mixed valence state of iron. Magnetite is known for its high permeability, which enhances its electromagnetic waves absorption capacity. Magnetite nanoparticles exhibit a high surface to volume ratio and by tuning synthesis parameters it is possible to control the particle size, shape and crystallinity. Consequently, these factors influence the magnetic, dielectric and loss properties. However, there are some drawbacks such as high mass density and limited dielectric losses that need to be addressed. In this view, the design of nanocomposites exhibiting both magnetic and electrical properties opens new interesting perspectives. Biomass-derived carbon-based materials are particularly useful in absorbing electromagnetic waves due to their lightweight nature and easy synthesis routes using cost-effective precursors. When the metal oxide is dispersed on the carbon matrix, the magnetic component induces impedance matching, increases the interfacial polarization, and enhances the electromagnetic waves absorption[30]. Keeping this in mind, in this study, the natural polymer apricot tree gum and activated carbonaceous porous structure obtained from oleaster seeds, were decorated with $Fe_3O_4$ nanoparticles. The microwave absorption properties of the triphasic composite were explored. Here, we have explored the properties of apricot tree gum decorated with magnetite for the first time, to the best of our knowledge. We specifically choose this biomaterial because apricot gums have a carbohydrate content ranging from 43.5% to 98.5%. Gums are polysaccharides in nature. Therefore, a higher proportion of carbohydrates may indicate a higher purity of the gum. A significant amount of moisture in powdered gums (17.50%) has been confirmed. Different polar functional groups create positive and negative charges in the molecule. The difference in electronegativity leads to the generation of dipoles in these charge centers. Specifically, through hydrogen bonding, O—H interacts and allows electrons to be transferred between different groups so that dipole polarization occurs[31]. In the presence of an alternating electromagnetic field, large polar functional groups increase dipole polarization and effectively dissipate electromagnetic energy. The presence of hydrogen bonds increases electrical conductivity. Hydrogen bonding in the polymer network plays the role of electron transfer which causes better impedance matching.

## 2 Experimental

### 2.1 Preparation of $Fe_3O_4$ (FE)

To prepare $Fe_3O_4$ nanoparticles, $FeCl_3·6H_2O$ and $FeCl_2·4H_2O$ with a molar ratio of 2 : 1 were dissolved in deionized water. The solution was placed in a heater and was completely dissolved using a magnetic stirrer. When the temperature reached 80 °C, NaOH was added. This solution was stirred for 30 min at the same temperature. Finally, the neodymium magnet was used to separate $Fe_3O_4$ nanoparticles after the solution had cooled[32].

### 2.2 Preparation of $Fe_3O_4$/activated carbon (FEOC)

All precursors used were of research grade and used without further purification. First, oleaster seeds were dried at 110 °C after activation with $ZnCl_2$. After evaporation of the excess water, the seeds were pyrolyzed under $N_2$ flow at a temperature of 700 °C and subsequently cooled to room temperature in a nitrogen atmosphere. The resulting carbon was then washed with HCl to reach a neutral pH value to obtain activated carbon (AC). In the second step, solutions of $FeCl_3·6H_2O$ and $FeCl_2·4H_2O$ were continuously stirred at 80 °C. After 30 min, AC was added to the solution, followed by NaOH solution that acted as a precipitant. Finally, the nanocomposite was washed with deionized water several times and separated using a neodymium magnet[27,33].

### 2.3 Preparation of $Fe_3O_4$/apricot tree gum resin (FEOR)

First, apricot tree gum (R) was soaked in deionized water. After drying, the gum was ground into powder using a mill and passed through a mesh to ensure uniformity. 2 g of powder was weighed and dispersed in deionized water. The resulting suspension was kept at room temperature for 24 h. Concurrently, a solution of iron salts was prepared following the same method described in section 2.2. The gum suspension was added to the metal salts solution under magnetic stirring, and the temperature of the combined solution was raised to 80 °C. After 15 min, Na-

OH was added to the solution. Finally, the nanocomposite was washed with water and the sediment was separated by a magnet.

### 2.4 Preparation of $Fe_3O_4$/activated carbon/apricot tree gum resin (FEOCR)

For this process, a suspension containing activated carbon and apricot tree gum resin in a 1∶1 mass ratio was prepared. Then the suspension was mixed with metal salt solution. The temperature was adjusted to 80 °C, and a NaOH agent was used for precipitation. Subsequently, the as-made nanocomposite was rinsed and air-dried at room temperature. Fig. 1 shows a schematic representation of the synthesis steps.

### 2.5 Characterization

The nanocomposites were analyzed by X-ray diffraction (XRD) using a TD-3700 model diffractometer, and by Fourier transform infrared (FTIR) spectrometry using a TENSOR 27 model spectrometer. Equations 1 and 2 were used to calculate $a$ (lattice constant) = 8.31 Å, and $V_{uc}$ (volume of the unit cell) = 573.85 Å:

$$a = d\left(h^2 + k^2 + l^2\right)^{1/2} \tag{1}$$

$$V_{uc} = a^3 \tag{2}$$

In these equations, $d$ represents the distance between the Bragg planes, which is obtained from Bragg's law, and $h$, $k$ and $l$ are Miller indices. The size of the crystallites ($D$) was obtained using the Debye-Scherrer equation.

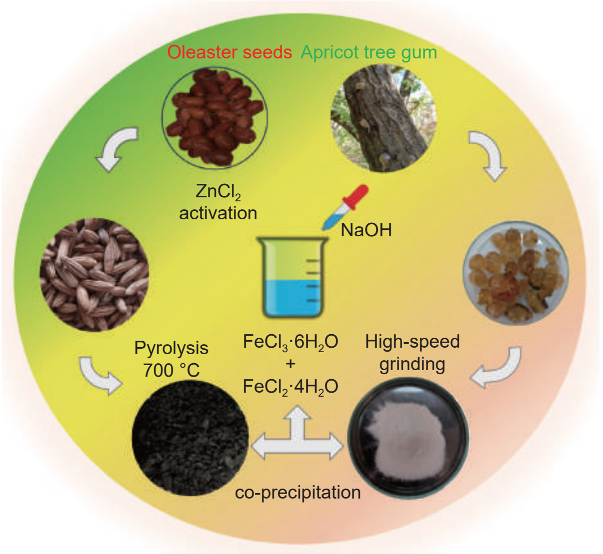

Fig. 1 Schematic illustration of the FEOCR nanocomposite synthesis method

$$D = \frac{0.89\lambda}{\beta\cos\theta} \tag{3}$$

In equation 3, $\lambda$, $\theta$ and $\beta$ are the wavelength of the X-ray used, Bragg angle, and peak width at half maximum, respectively.

The morphology of the nanostructures and chemical compositions was investigated using a MIRA3-TESCAN field emission scanning electron microscope (FESEM) equipped with energy dispersive X-ray spectrometer (EDS). Magnetic properties were measured using a vibrating sample magnetometer (VSM) from Maghnatis Daghigh Kavir Co., Iran. Raman spectroscopy (Horiba Jobin-Yvon Labram HR800) was used to investigate the geometrical structure and bonding within the molecules. The analysis of the surface area was done by Brunauer–Emmett–Teller (BET) method using the equipment BELSORP Mini II made in Japan. X-ray photoelectron spectrometer (XPS, PHI QUANTERA II) with Al K-alpha source was used to analyze the elemental composition of the composites.

The nanocomposites were homogeneously mixed with paraffin wax to evaluate their microwave absorption properties. A vector network analyzer (VNA) was employed to analyze the electromagnetic parameters of the samples, using a WR90 waveguide at $f$ = 8–12 GHz. The WR90 waveguide has a rectangular shape with dimensions of 10.16 mm × 22.86 mm. The composite samples were thoroughly dispersed in a paraffin matrix with a 1∶3 mass ratio. Finally, the samples were separately poured into an aluminum mold to fabricate the samples used to test microwave absorption.

## 3 Results and discussion

The X-ray diffraction (XRD) patterns of the magnetic nanocomposites prepared by the co-precipitation method are shown in Fig. 2a. The FEOC and FEOCR samples show a broad amorphous hump in the range of $2\theta$ = 20°–30°, which can be ascribed to amorphous carbon. In the FEOC sample, this broad peak is more prominent due to the higher weight per-

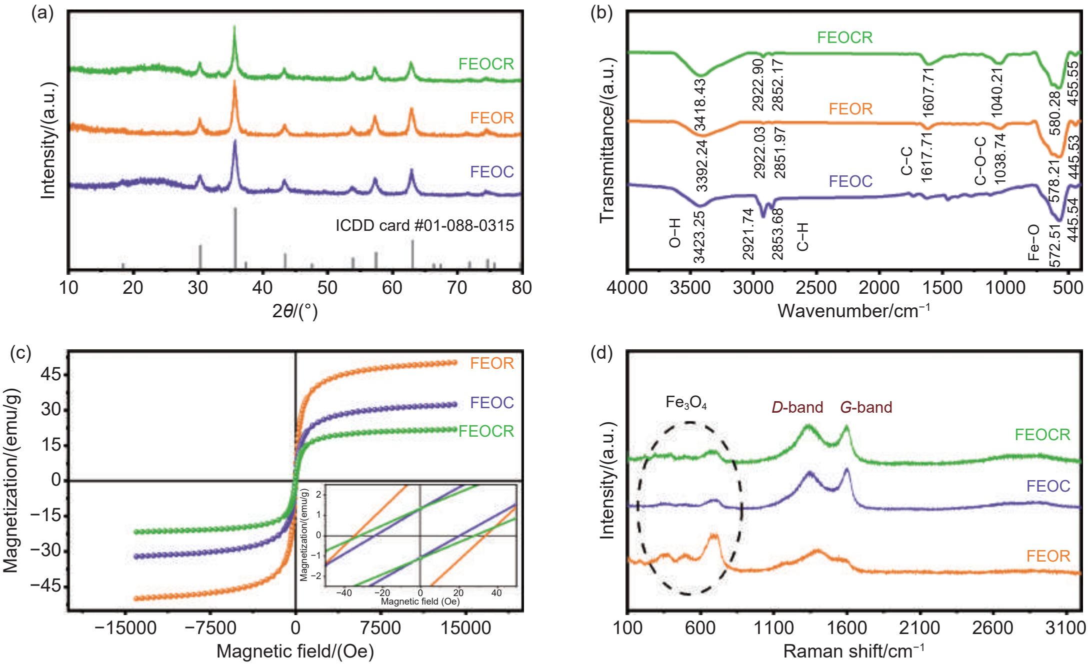

Fig. 2　(a) XRD patterns, (b) FTIR spectra, (c) Magnetic hysteresis loops (inset shows low-field data), and (d) Raman spectra of the nanocomposites

centage of carbonized material as compared with FEOR sample. The Bragg reflections testify that the ferrite nanoparticles obtained by this method have a spinel cubic structure (ICDD card #01-088-0315). The average crystallite size of $Fe_3O_4$ nanoparticles in FEOC, FEOR and FEOCR composites were calculated to be 10.3 (±0.8), 10.6 (±0.7), and 11.8 (±0.9) nm, respectively.

The chemical species in the nanocomposites were evaluated by FTIR. As indicated in Fig. 2b, the O—H bond is noticeable at ~3 400 $cm^{-1}$. The observed twin peaks at 2 920 and 2 850 $cm^{-1}$ are related to the C—H bonds. The peaks below 1 000 $cm^{-1}$ are ascribed to $Fe_3O_4$. The notches at 572 and 445 $cm^{-1}$ are related to (Fe-O) bonds, with Fe located in the octahedral and tetrahedral sites, respectively[34]. The observed peaks could originate from the organic functional groups existing in the composites.

Magnetic parameters play a crucial role in the wave absorption and performance. The magnetic hysteresis loops recorded at 300 K are shown in Fig. 2c. The saturation magnetization of FEOR (~50 emu/g) is larger than that of FEOC (~32 emu/g) and FEOCR (22 emu/g). Notably, the value of $M_S$ has a direct effect on the magnetic permeability and impedance matching, which in turn affect the wave absorption performance. The coercivity values ($H_C$) for the FEOR, FEOC, and FEOCR composites are ~35, ~20 and ~30 Oe, respectively. Large values of $H_C$ and $M_S$ can improve magnetic loss. This can be easily seen from the fact that the area of the curve gives the energy required to complete one magnetization and demagnetization cycle, and the energy loss is equal to the area of the loop.

To further investigate the growth of the nanoparticles on the resin and carbon matrix, Raman spectroscopy was used to analyze the molecular structures and identify the chemical composition in the samples. The dielectric parameters and their effect on the microwave absorption capacity are significantly affected by the conjugated structures in the composites. In Fig. 2d, the main peak of Raman scattering for ferrite is observed at 670 $cm^{-1}$, which corresponds to A1g vibrational mode of the spinel structure. In addition, the peaks at approximately 1 330 and 1 595 $cm^{-1}$ correspond to the *D* and *G* bands, respectively. This confirms the presence of carbon in the nanocomposites[35]. The *D* band shows the presence of distortion and lattice defects of carbon atoms, which are related to $sp^3$ lattice disorders in the amorphous carbon, acting as polarization centers under the incident microwaves[36,37]. The *G* band arises from the structure of graphite and can be attributed to the stretching vibrations of the sp$^2$ hexagonal graphite lattice. Notably, defects and impurities in the structure affect the position of the peaks. The ratio ($I_G/I_D$) was used to determine the degree of irregularity and evaluate the uniformity by multiple measurements at different locations of the material. $I_G/I_D$ values for FEOR, FEOC, and FEOCR composites are 0.65, 1.11 and 0.97, respectively. Defects cause the creation of many polarization centers, which ultimately attenuate the incident microwaves. Interestingly, the presence of resin reduces the $I_G/I_D$ value which may affect microwave absorption through defect centers.

Next, the morphology of the FEOC FEOR, and FEOCR nanocomposites was investigated using FESEM (Fig. 3). Fig. 3a shows an image of activated carbon derived from oleaster seeds. Fig. 3b shows an image of the gum particles, revealing particle sizes mostly greater than 100 μm. This natural resin can be dissolved in water, which makes the dispersion of magnetic nanoparticles more homogenous in the carbon matrix. This is seen in Fig. 3c, where the $Fe_3O_4$ nanoparticles with spherical structures are well dispersed in the gum matrix, resulting in a uniform morphology of the FEOR composite (see inset in Fig. 3c). In contrast, in the FEOC sample (Fig. 3d), the dispersion of the $Fe_3O_4$ nanoparticles on the carbon surface is poor, with some areas having no magnetic nanoparticles on the surface of the activated carbon. For the FEOCR composite (Fig. 3e), it is observed that the $Fe_3O_4$ nanoparticles and gum are distributed on the pyrolyzed carbon structure. The EDS elemental mapping of the FEOCR sample (Fig. 3f) confirms the presence of Fe, O and C in the composite. The use of

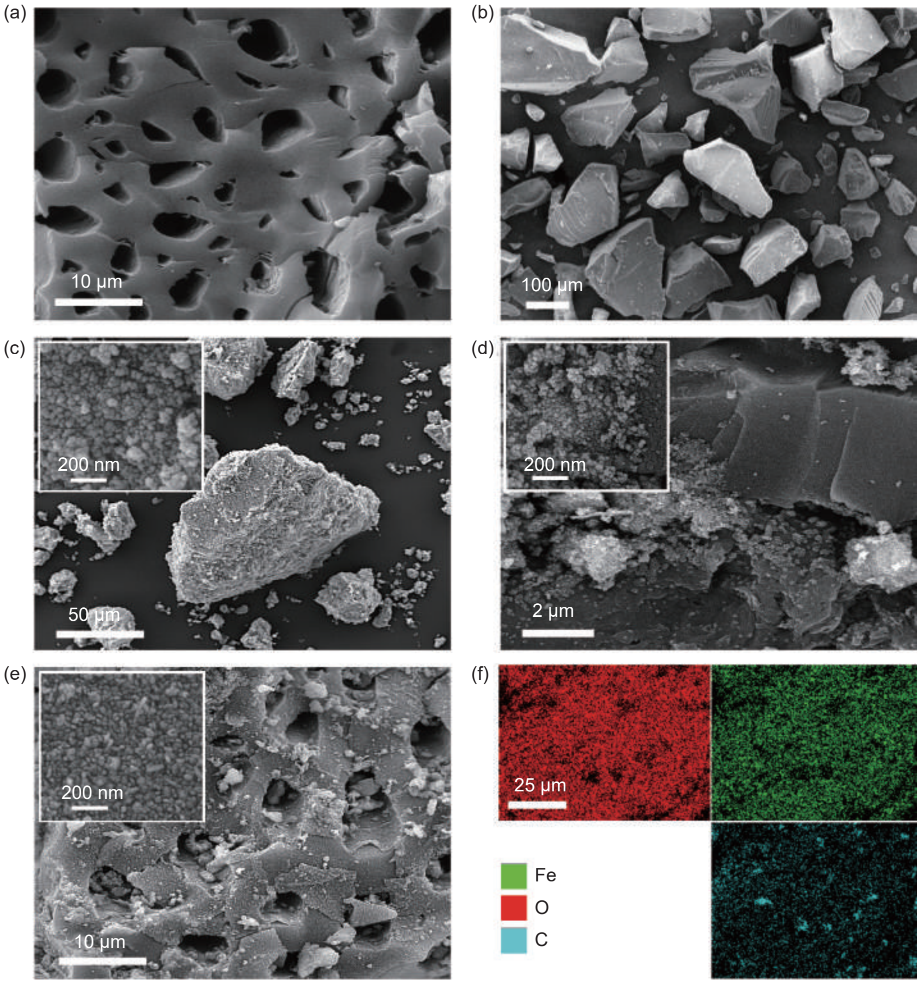

Fig. 3 FESEM images of (a) activated carbon derived from oleaster seeds, (b) Apricot tree gum, (c) FEOR, (d) FEOC and (e) FEOCR nanocomposites. Insets in (c-e) are magnified images showing $Fe_3O_4$ nanoparticles. (f) EDS elemental mapping of FEOCR sample

natural resin during the synthesis process results in a uniform distribution of $Fe_3O_4$ particles on the carbon surface.

Nitrogen adsorption allows to investigate the porosity and specific surface area of samples. This test method is based on surface absorption and involves measuring the volume of nitrogen gas absorbed and desorbed by the surface of the material at a constant temperature[38]. The cell containing FEOC, FEOR and FEOCR samples were placed in a tank at a constant temperature and by gradually increasing and then decreasing the pressure of the carrier gas, the amount of gas absorbed and desorbed by the material was calculated. The specific surface area, volume and size distribution of the nanocomposites could be calculated, which are listed in Table 1. Fig. 4a and b show the nitrogen ($N_2$) adsorption/desorption isotherms and pore size distribution curves. These curves indicate a type IV isotherm, which contains pores smaller than 2 nm (i.e., micropore), as well as pores between 2 and 50 nm (i.e., mesopores). The specific surface areas of the FEOC, FEOR and FEOCR samples are 814.2[27], 67.3 and 431.9 $m^2g^{-1}$, respectively. The corresponding total pore volumes of the samples are 0.05, 0.25 and 0.16 $cm^3g^{-1}$ and the corresponding average sizes of the pores are 1.21, 3.53 and 1.21 nm. It is not surprising that after the introduction of apricot tree gum, the surface area and the volume of the pores decrease greatly[39]. The pore size distribution curves of FEOC and FEOCR show a mean value of 1.21 nm, which indicates the presence of micropores in the samples.

Fig. 5 shows the XPS results of the FEOCR sample. The survey scan (Fig. 5a) depicts the Fe 2p, C 1s and O 1s characteristic peaks, showing the presence of Fe, C and O elements in the composite, which is in accordance with the EDS mapping results. For more information, high-resolution spectra are acquired. The high-resolution experimental spectrum of Fe 2p (Fig. 5b) shows 2 peaks related to Fe $2p_{1/2}$ and Fe $2p_{3/2}$ spin-orbit coupling, further confirming the existence of $Fe_3O_4$ in the composite. The binding energies of 710.7 and 724.1 eV correspond to $Fe^{2+}$ $2p_{3/2}$ and $Fe^{2+}$ $2p_{1/2}$, respectively, while the peaks at 712.5 and 726.0 eV correspond to $Fe^{3+}$ $2p_{3/2}$ and $Fe^{3+}$ $2p_{1/2}$, respectively. A satellite peak is observed at 719.3 eV. Fig. 5c shows the C 1s high-resolution spectrum, where 3 distinct peaks corresponding to C—C/C═C (284.8 eV), C—O (286.6 eV), and C═O (288.4 eV) bonds are observed[40]. The O 1s peak at 530.2 eV (Fig. 5d) corresponds to Fe—O bonds, in which the O represents the spinel lattice oxygen[41,42]. The signals at 531.4 and 533.0 eV originate from O═C and O—C bonds, respectively.

Time-varying electromagnetic waves propagate

**Table 1 Results of nitrogen absorption and desorption**

| Samples | $V_m$/($cm^3$(STP)$g^{-1}$) | $a_{S,\,BET}$/$m^2$ | $r_p$/nm | $V_p$/($cm^3g^{-1}$) | References |
|---|---|---|---|---|---|
| FEOC | 187.06 | 814.2 | 1.21 | 0.05 | [27] |
| FEOR | 15.45 | 67.3 | 3.53 | 0.25 | This work |
| FEOCR | 99.23 | 431.9 | 1.21 | 0.16 | This work |

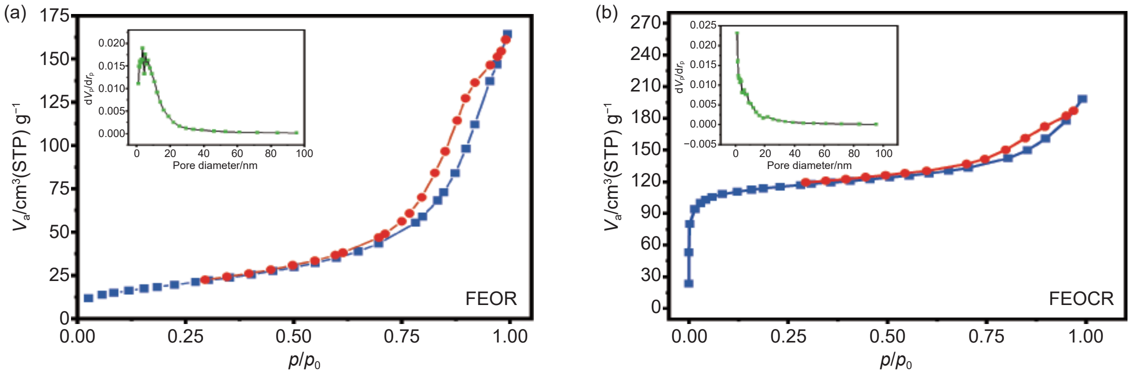

Fig. 4 $N_2$ adsorption−desorption isotherms and the pore size distribution curves of (a) FEOR and (b) FEOCR nanocomposites

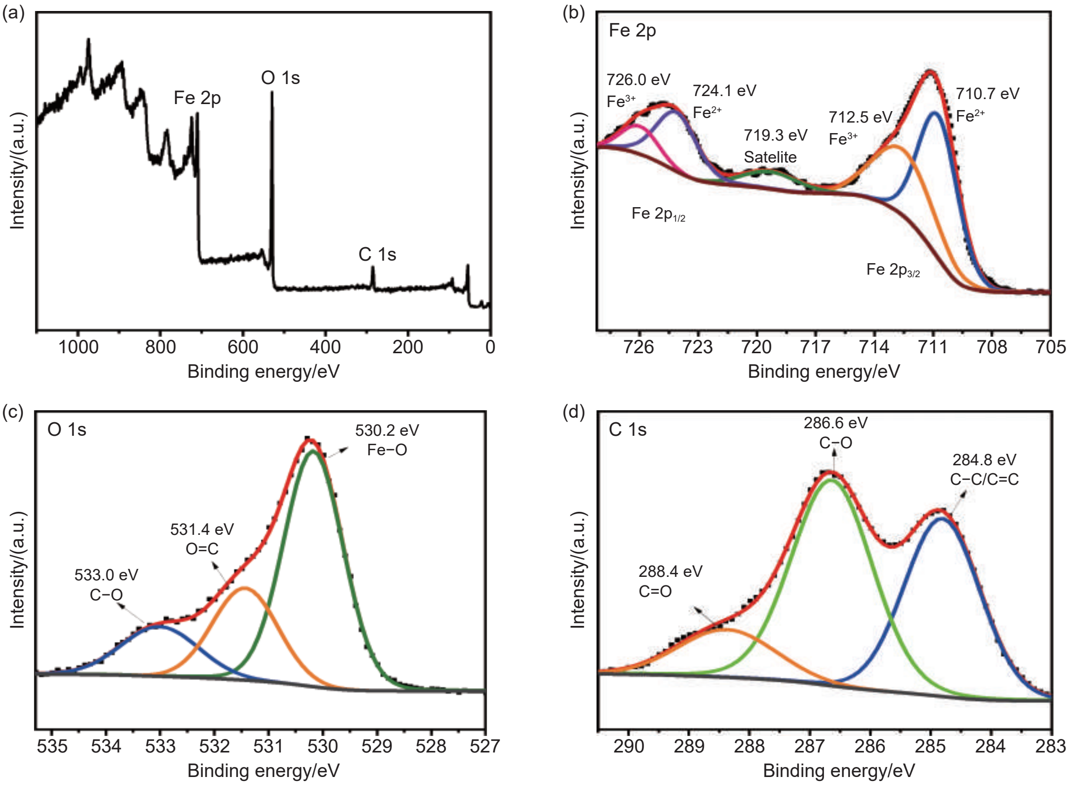

Fig. 5 XPS spectra of FEOCR composite. (a) Survey scan, and high-resolution spectra of (b) F 2p, (c) O 1s and (d) C 1s

over long distances like a plane wave, and the electric and magnetic fields are perpendicular to the direction of propagation. Therefore, two basic parameters, namely, relative permittivity ($\varepsilon_r$) and magnetic permeability ($\mu_r$) of the nanocomposites should be investigated[43,44].

$$\varepsilon_r = \varepsilon' - j\varepsilon'' \tag{4}$$

$$\mu_r = \mu' - j\mu'' \tag{5}$$

where $\varepsilon'$ and $\mu'$ are related to the storage capacity (Fig. 6a and c), and $\varepsilon''$ and $\mu''$ give information about the energy losses (Fig. 6b and d)[45]. For high absorption, both magnetic and dielectric losses in the absorbing materials need to be increased. When a carbonaceous material is composited with a ferrite, the permittivity is enhanced with respect to the ferrite[46]. This enhancement is due to the conductive and relaxation loss that arises from the carbonaceous structure. By analyzing the data of the electrical and magnetic parameters, the impedance matching can be evaluated[47]. The fluctuation in the electric and magnetic parameters leads to the observation of a resonant peak. Resonance peaks in permittivity curves are usually caused by interfacial and dipolar polarizations[48,49]. The defects and holes existing in the composite structure enhance the polarization. In Fig. 6a and b, it is observed that the values of $\varepsilon'$ and $\varepsilon''$ remain unchanged for FE, FEOR, FEOC and FEOCR nanocomposites, and FEOR has the lowest value among the 3 samples. FEOC and FEOCR nanocomposites have higher $\varepsilon'$ and $\varepsilon''$ values as compared with FE, which may be related to the presence of a larger number of polarization sites and improved conductivity due to the presence of activated carbon. As seen from Fig. 6c and d, the curves of $\mu'$ and $\mu''$ are in the range of 0.9–1.1 and 0.002–0.1, respectively. The magnetic behavior is tuned through the dielectric behaviors of the gum and activated carbon due to interfacial coupling between the different components[50,51]. Due to the impact of electromagnetic wave radiation on FE, FEOR, FEOC and FEOCR nanocomposites, an alternating electric field is created by the movement of the internal charge, which induces a magnetic field inside the material. For the $\mu'$ curve of FEOR nanocomposite, an extreme value is seen in the frequency range of 8–12 GHz. As seen in the $\mu''$ curve of FEOR nanocomposite, the maximum value is obtained at 10.8 GHz,

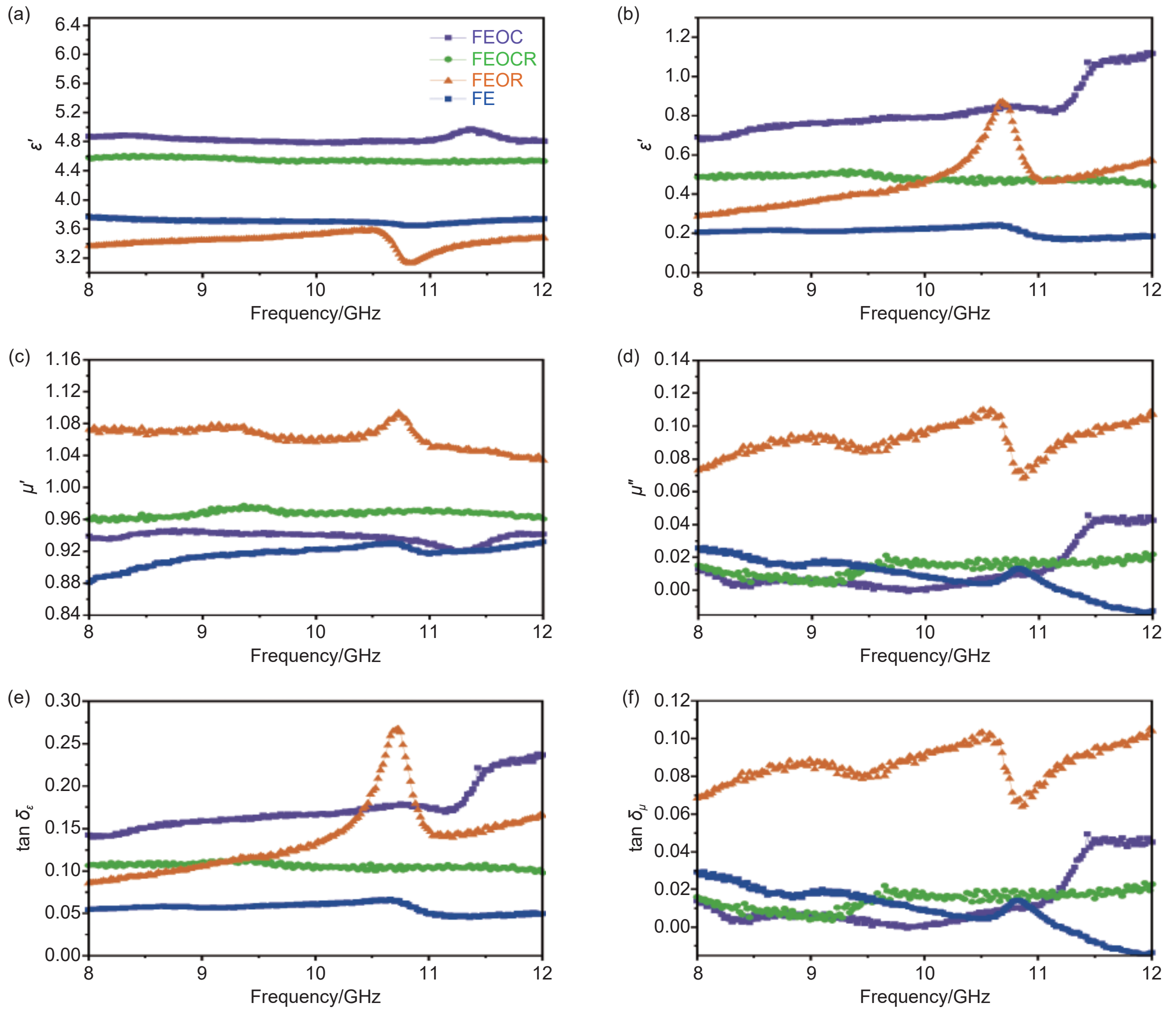

Fig. 6　(a) $\varepsilon'$ and (b) $\varepsilon''$, (c) $\mu'$ and (d) $\mu''$, (e) tan $\delta_\varepsilon$ and (f) tan $\delta_\mu$ versus frequency for 4 samples

which indicates an increased magnetic loss in this sample compared to FE, FEOC and FEOCR samples under the influence of ferromagnetic resonance.

The relation $\tan\delta_\varepsilon = \varepsilon''/\varepsilon'$, and $\tan\delta_\mu = \mu''/\mu'$ show the dielectric and magnetic loss, respectively (Fig. 6e and f). The values of $\delta_\varepsilon$ and $\delta_\mu$ determine the role of losses in the microwave absorption process. The results show that the intensity of the dielectric loss of the nanocomposites is higher than the intensity of the magnetic loss, suggesting that dielectric losses have a more significant effect on microwave absorption than magnetic losses. It is obvious that each of these samples shows multiple variation trends in the frequency range of 2–8 GHz for the imaginary parts of permeability and permittivity. This is because the imaginary parts related to permeability and permittivity are the key parameters affecting the magnetic loss and dielectric loss, respectively.

According to the transmission line theory and its generalization to electromagnetics, and the calculation of impedance ($Z_{in}$), it is possible to define the reflection loss (RL) related to the performance of the absorber[52].

$$Z_{in} = Z_0\sqrt{\frac{\mu_r}{\varepsilon_r}}\tanh\left(j\frac{2\pi f t}{c}\sqrt{\mu_r\varepsilon_r}\right) \tag{6}$$

$$\mathrm{RL} = 20\log\left|\frac{Z_{in}-Z_0}{Z_{in}+Z_0}\right| \tag{7}$$

where, $Z_0$ is the impedance of free space (377 Ω), $c$ is the speed of the wave, $f$ is the frequency and $t$ is the thickness of the prepared sample.

A proper selection of the absorber material is crucial for achieving superior absorption in low thickness and wide bandwidth. Absorption of 90% is encountered when the reflection loss is less than −10 dB. Fig. 7 shows the frequency dependence of the reflection loss in the X-band for the samples at different thicknesses.

The behaviors of the nanocomposites (Fig. 7c-h) are compared with that of pure magnetite (Fig. 7a and b). As seen in Fig. 7c and d, for the FEOC sample, the reflection loss at 9.69 GHz with a thickness of 1 mm is −51.12 dB, which is much larger than that for FE (−13.03 at 10.79 GHz). The highly porous structure of activated carbon can facilitate multiple reflections and scattering of the propagated microwaves, thereby attenuating their intensity and converting them to thermal energy. Also, the nucleation of $Fe_3O_4$ filler in the matrix is expected to improve microwave absorption by increasing the relaxation loss and reflections. However, better results are expected when the nanoparticles are homogeneously dispersed in the matrix without any significant aggregation. In addition, the $Fe_3O_4$ particles are highly insulating and thus can suppress the negative effects of eddy current, which adversely affects the absorption of microwaves. For the

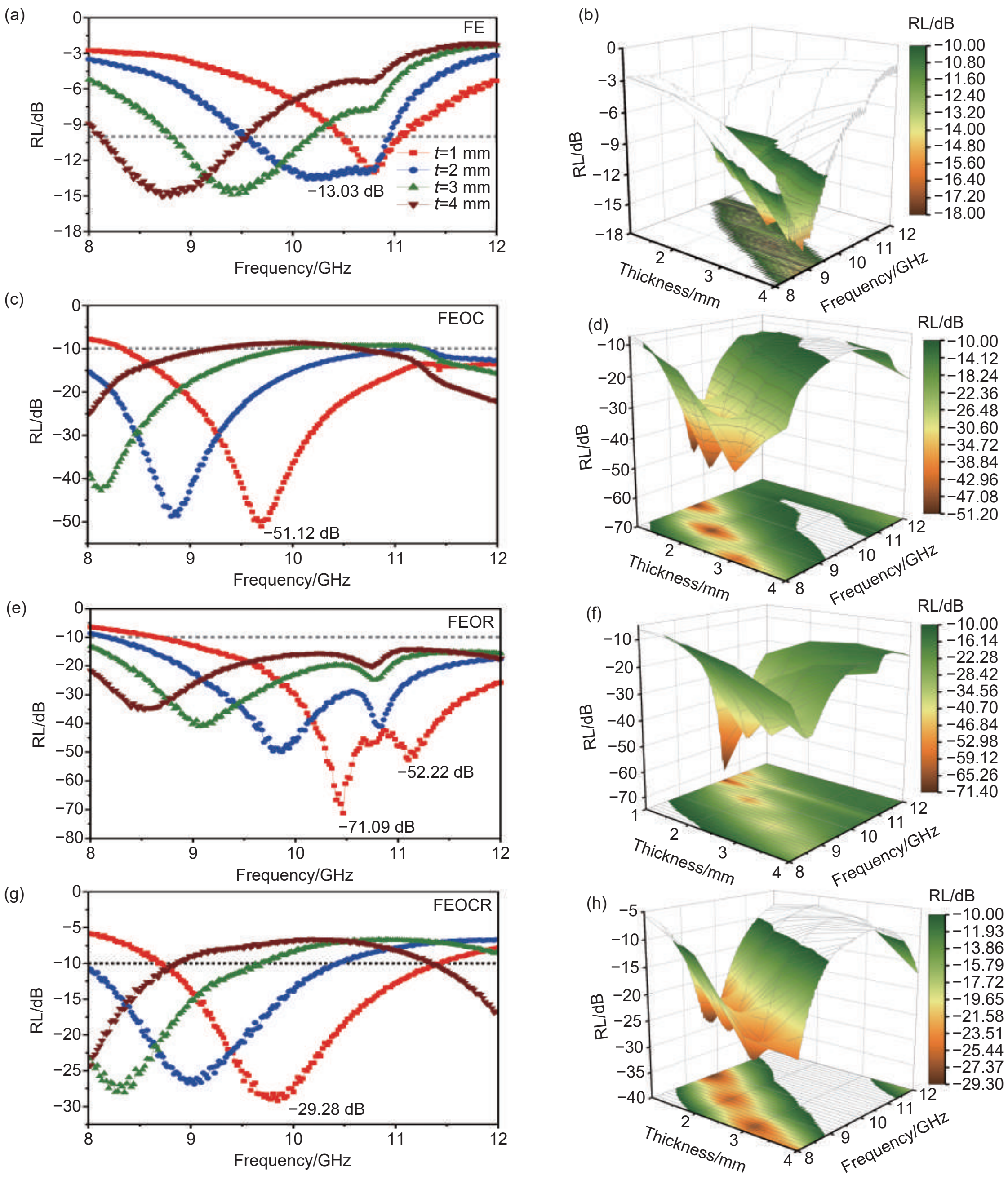

Fig. 7 RL curves and 3-D contour maps of (a,b) FE, (c,d) FEOC, (e,f) FEOR and (g,h) FEOCR samples

FEOR sample (Fig. 7e and f), a superior reflection loss (RL = −71.09 dB) occurs at 10.45 GHz for $t$ = 1 mm. The available bandwidth in the X-band range is 3.36 GHz, which increases to 3.83 GHz for thickness $t$ = 2 mm. Interestingly, the effective absorption bandwidth of FEOR increases with vacancy defects. First principle calculations provide evidence that vacancy defects lead to a change in the electric dipole state, leading to a more effective absorption bandwidth[53]. On the other hand, the FEOCR sample shows RL = −29.28 dB at $f$ = 9.85 GHz (Fig. 7g and h). The addition of gum to the FEOC structure reduces the amount of reflection loss. Thus, the FEOR sample demonstrates the highest reflection loss and covers the entire X-band for $t$ = 2 mm. The maximum RL intensities and absorption bandwidths of different biomass-based composites are listed in Table 2 for comparison with the current study.

In this work, the effects of apricot tree gum on microwave absorption performance were investigated. The results show that the presence of apricot tree gum has a significant effect on bandwidth and reflection losses. In addition, in the FEOCR nanocomposite, the minimum reflection loss has decreased while covering almost the entire X-band, which can be attributed to the increase in conductivity due to activated carbon. The microwave absorption curves show that FEOR and FEOCR composites have the strongest reflection loss in the frequency range of 8–12 GHz. On the other hand, apricot tree gum and $Fe_3O_4$ nanoparticles can drastically change the surface conditions. These changes in the interface between $Fe_3O_4$ and apricot tree gum can be due to the phenomenon of dielectric/magnetic resonance[54]. The presence of interfaces in this nanocomposite causes surface polarization and resonant behavior.

The performance of electromagnetic wave absorbers can be maximized when the incident wave has the lowest reflection from the interface and the highest transmission inside the absorber structure[55]. This can be achieved by tuning the impedance of the absorber. The relative impedance ($|Z_{in}/Z_0|$) is an important parameter, and in the ideal case when the impedance matching value is equal to one, the electromagnetic wave can completely penetrate the material[56]. Relative impedance matching $|Z_{in}/Z_0|$ implies that the resin can augment the impedance matching in the FEOR conjugated structure (Fig. 8). From Fig. 8b, d, and f, the ideal impedance matching ($|Z_{in}/Z_0|=1$) areas are detectable for all the composites (denoted by the dashed lines). By comparing the results presented in Fig. 7, it is observed that FEOR has the best impedance matching, and shows the highest absorption through losses.

The closer the values of $\varepsilon_r$ and $\mu_r$ are, the less reflection there will be and the greater the reflection loss of the electromagnetic wave. To obtain effective electromagnetic wave absorption, there must be an effective complement between dielectric and magnetic

**Table 2　Comparison of EM wave absorption abilities of different biomass-derived materials**

| Origin | Boostingagent | Max. RL/dB | Efficient bandwidth/GHz | Matching thickness/mm | Ref. |
|---|---|---|---|---|---|
| Mature platanus | 3D magnetic (Co) porous carbon fibers with a helical/chiral structure | −61.1 | 2.1 | 3.9 | [84] |
| Shaddock peels | $Fe_3O_4$/porous carbon nanosheets | −50.3 | 2.0 | 3.5 | [85] |
| Chicken Featherfibers | Porous carbon/epoxy | −20.1 | 2.9 | 2.0 | [86] |
| Eggshell membrane | C@$CoFe_2O_4$ | −49.6 | 3.0 | 2.5 | [87] |
| Wheat straw | $Fe_3O_4$@ Fe/carbon foam | −43.6 | 2.8 | 4.7 | [88] |
| Jackfruit peel | $Ni(OH)_2$/activated carbon | −23 | 1.9 | 5.5 | [89] |
| Flour dough | Hierarchically porous carbon | −52 | 2.4 | 2.5 | [90] |
| Peach gum (NPG) | Porous carbon | −59.4 | 4.1 | 2.0 | [91] |
| Eucommia ulmoides gum (EUG) | Carbon nanotube (CNT)/graphene nanoplatelet (GNP)/EUG | −42.5 | 2.7 | 2.0 | [92] |
| Oleaster seed (C) | FEOC | −51.1 | 3.7 | 1 | [27] |
| Apricot tree gum (R) | FEOR | −71.1 | 3.3 | 1 | This work |
| C/R | FEOCR | −29.3 | 2.8 | 1 | This work |

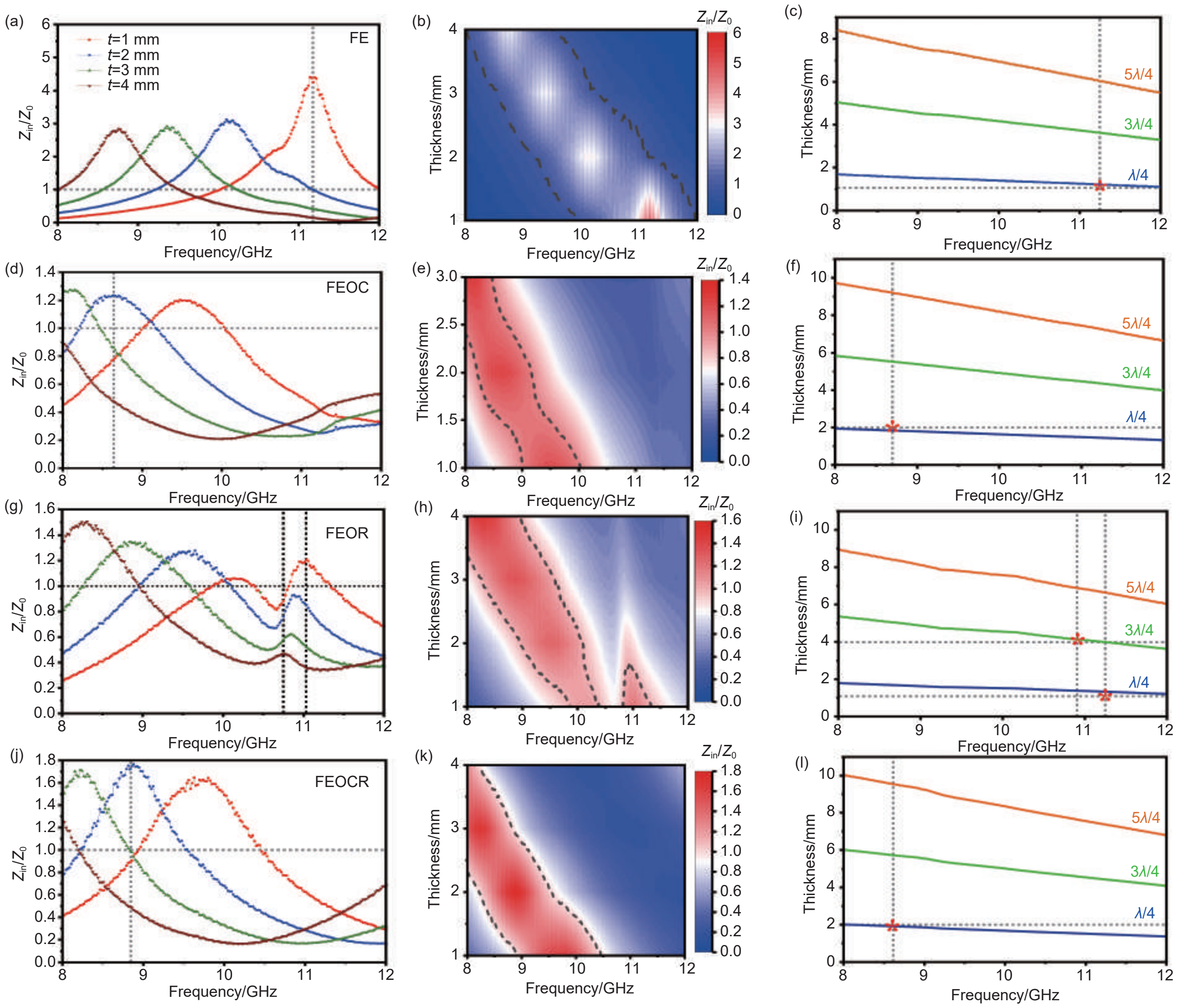

Fig. 8 Impedance and 2-D mapping plots of $Z_{in}/Z_0$ values at different thicknesses and the corresponding theoretical matching thickness for (a,b) FE, (c,d) FEOC, (e,f) FEOR and (g,h) FEOCR nanocomposites

losses to achieve certain impedance characteristics[57]. When $Z_{in}/Z_0$ is equal to or close to 1, the electromagnetic waves are not reflected from the surface of the absorbing material and are instead absorbed inside the nanocomposite. At this time, the absolute value of reflection loss reaches the maximum value[58]. Impedance matching in samples FEOC, FEOR and FEOCR are all close to 1 in contrast to pure magnetite. In the FEOR sample, the $Z_{in}/Z_0$ value reaches its minimum value (1.05) for the thickness of 1 mm, which shows a high reflection loss value. If the impedances are mismatched, most of the incident waves will be reflected from surface or transmited through the material without any loss, resulting in poor RL. It can be seen that the synergistic effect between the dielectric and magnetic properties leads to good matching and damping inside the electromagnetic wave absorber, resulting in very good wave absorption characteristics.

As seen in Fig. 7, as the amount of absorber and sample thickness increasing, $RL_{min}$ values move towards a lower frequency. This is expected because the frequency is inversely proportional to the thickness of the absorber. Therefore, this function can be explored using the quarter-wavelength theory (Fig. 8c, f, i and l). The relationship between coating thickness ($t_m$) and matching frequency ($f_m$) is expressed as the following equation[59]:

$$t_m = \frac{nc}{4f_m\sqrt{|\mu_r\varepsilon_r|}} \quad (n = 1,2,3,\cdots) \tag{8}$$

where $t_m$ is the thickness of the absorber, $f_m$ is the matching frequency with $RL_{min}$, and the values of $c$, $\mu_r$, and $\varepsilon_r$ are already defined. Electromagnetic wave energy is absorbed through various mechanisms, and one of the mechanisms is phase elimination. When an electromagnetic wave passes through the absorber, part of the wave is reflected at the air-absorber interface, and the rest is transmitted or multi-reflected inside the absorber. At some frequencies, the thickness of the absorber is equal to a quarter of the transverse wavelength. When this happens, the reflected waves are out of phase with the incident waves, canceling both waves. This destructive interference leads to attenuation of the electromagnetic wave signals, at this point the maximum absorption is indicated by $RL_{min}$ in the response[60]. This maximum absorption occurs when the absorber thickness $t_m$ is equal to $\lambda_m/4$, where $\lambda_m$ is the effective wavelength of the electromagnetic signal inside the material and $\lambda_0$ is the free space wavelength described by the equation[61]:

$$\lambda_m = \frac{\lambda_0}{\sqrt{|\mu_r \varepsilon_r|}} \tag{9}$$

In summary, the resonant frequency decreases with increasing the absorber thickness due to this condition of $\lambda/4$, while RL decreases, indicating an increase in EM wave absorption.

Fig. 9 shows the Cole-Cole plots for the samples. These plots provide information about the type of polarization in the samples, obtained from the Debye relaxation theory[62,63].

$$\left(\varepsilon' - \frac{\varepsilon_s + \varepsilon_\infty}{2}\right)^2 + (\varepsilon'')^2 = \left(\frac{\varepsilon_s - \varepsilon_\infty}{2}\right)^2 \tag{10}$$

Here, $\varepsilon_\infty$ represents the permittivity at $f = \infty$, and $\varepsilon_s$ is the static permittivity. The individual semicircles in the plots of Fig. 9 show that the Debye relaxation process exists. The defects, crystal dislocations, and functional groups cause the relaxation. Thus, functional groups and defects on the surface cause the formation of semicircles. Polarization effects can arise from surface, dipole, ionic and/or electron polarization. Ionic polarization occurs below $10^5$ Hz and dipole polarization below $10^6$ Hz. According to the Fig. 9, the FEOC and FEOCR samples have a larger number of semicircles than FEOR, which is due to surface and dipole polarizations and residual functional groups such as O—H and C=C bonds[64,65]. The phenomenon of polarization relaxation can be attributed to the

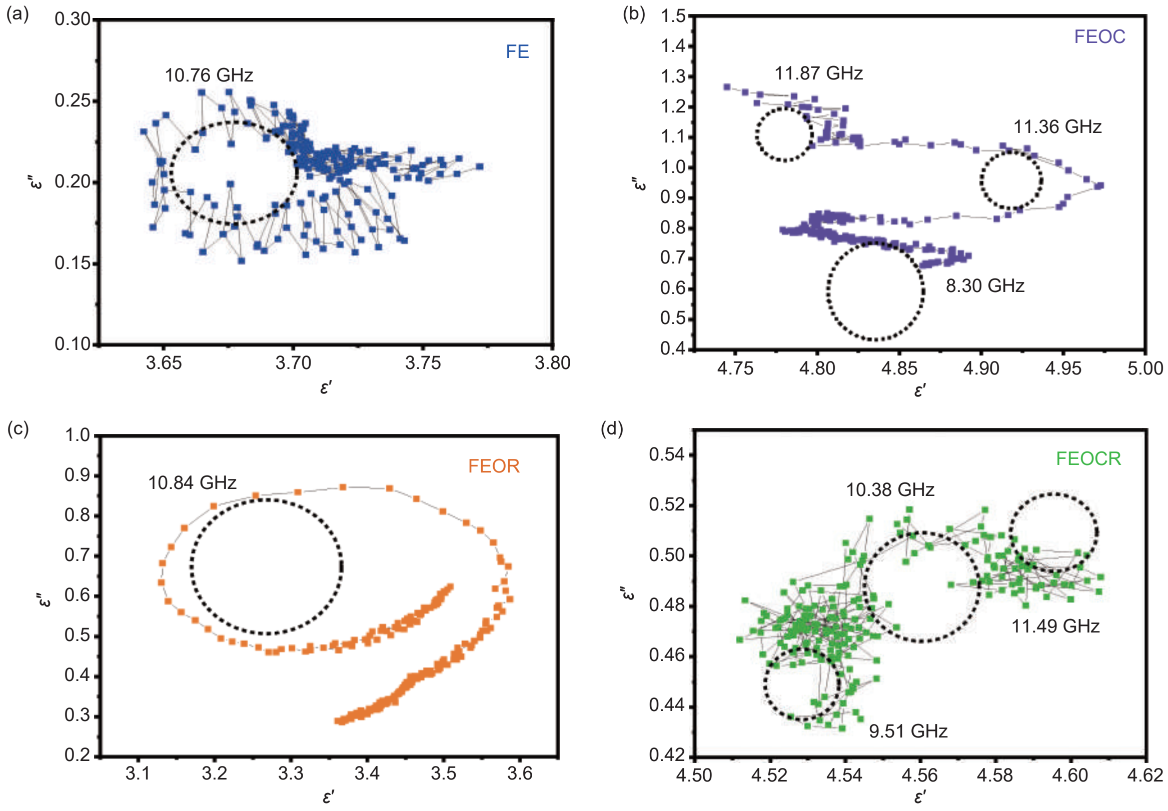

Fig. 9 Cole-Cole plots of FE and the nanocomposites

relaxation of dipole polarization, Maxwell-Wagner effect caused by multiple dangling atoms, polarization caused by an induced electric field, along with many surface defects, which can enhance the high absorption property of microwaves[66,67]. The larger number of semicircles observed in Fig. 9b and d indicates a better electromagnetic discharge capacity of the corresponding samples and the presence of multiple dielectric polarization processes. Fig. 9a and c show only one semicircle, which could be related to the dielectric loss. Also, porous structures cause polarization on the nanocomposite surface by creating interfaces. Therefore, it can be concluded that surface defects in nanocomposites represent a reasonable mechanism to explain the microwave absorption performance. Complex polarization processes and other forms of polarization relaxation may sometimes occur in composites during the absorption of electromagnetic waves[68]. In this case, the Cole-Cole plots consist of more than one semicircle, which might also be distorted. The Cole-Cole plots of FEOC and FEOCR nanocomposites are observed to consist of 3 semicircles in different frequency bands, which correspond to the frequency range where the reflection loss occurs[69]. In the frequency range of FEOC and FEOCR nanocomposites, the first semicircle is related to multiple relaxation processes. However, the rest arises from the loss of conductivity. Therefore, simultaneous dipole and interface polarization occur between 8 and 12 GHz. Various heterogeneous interfaces in FEOC and FEOCR composites, including carbon-air, carbon-metal and air-metal interfaces, cause strong surface polarization. The porous carbon skeleton forms an interconnected conductor. Therefore, it can be concluded that carbon materials absorb electromagnetic waves with combined polarization relaxation and conduction losses.

In addition, high magnetic permeability is another essential parameter for increasing microwave attenuation, which is related to eddy current losses and ferromagnetic resonance. Losses related to eddy currents exist if the parameter $C_0 = \mu''\mu'^{-2}f^{-1}$ remains constant in the frequency interval[70]. As can be seen in Fig. 10a, for FEOCR, the value of $C_0$ decreases slightly in the frequency range of 8–9.25 GHz, followed by a slight increase, after which it remains constant in the frequency range of 9.5–12 GHz. For ferrimagnetic materials, in the gigahertz frequencies, the main magnetic losses arise from natural ferromagnetic resonance and the eddy current[70]. Therefore, for the composite samples the main sources of magnetic losses are the natural resonance and the eddy current.

To investigate and analyze the overall attenuation rate of the absorber, the attenuation constant ($\alpha$) is calculated using the following equation[71].

$$\alpha = \frac{\sqrt{2}\pi f}{c}\sqrt{(\mu''\varepsilon'' - \mu'\varepsilon') + \sqrt{(\mu''\varepsilon'' - \mu'\varepsilon')^2 + (\mu'\varepsilon'' + \mu''\varepsilon)'^2}} \tag{11}$$

For the FEOC sample, the value of $\alpha$ increases from 135.86 to 214.09 Np/m, for the FEOR sample from 66.55 to 108.18 Np/m, and for the FEOCR sample from 119.79 to 176.72 Np/m (Fig. 10b) with increasing frequency. At higher frequencies, the attenuation rate is higher due to increased dielectric losses.

Finally, the radar cross-section (RCS) was meas-

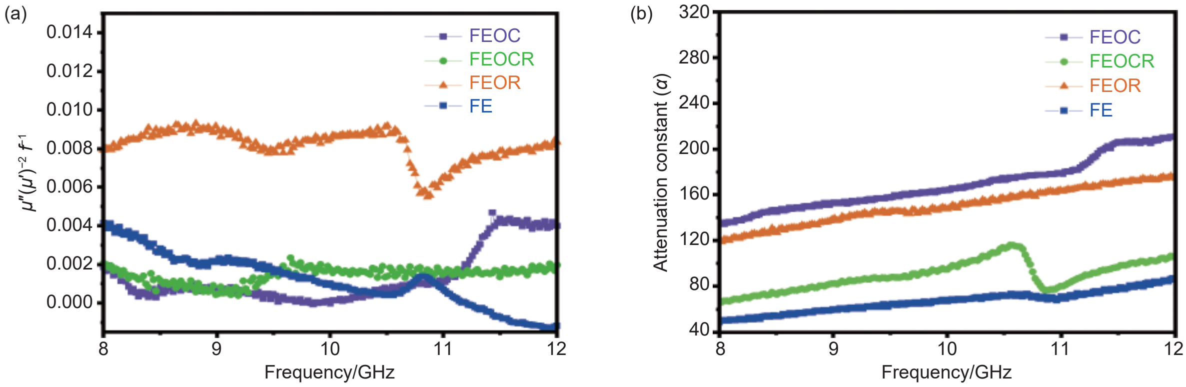

Fig. 10　(a) $C_0$-$f$ curves and (b) attenuation constant of the samples ured using computer simulation (CST). The results are summarized in Fig. 11. The CST results show that the perfect conductive layer (PEC) shows the strongest scattering signal[72,73]. The PEC coated by FEOC, FEOR and FEOCR nanocomposites show a much higher signal intensity than that coated with a thickness of 1 mm. These contrasting results further prove that most of the electromagnetic energy is effectively attenuated by the heterogeneity of apricot tree gum and carbon. In comparison, the obtained FEOR sample shows the lowest RCS values (less than 10 dB $m^2$) in the full range of 0–360° (Fig. 11), which corresponds well with the prominent electromagnetic absorption properties. On the other hand, almost all 3 nanocomposites have significant radar stealth properties compared to PEC for practical applications.

The possible mechanisms causing the microwave absorption in the nanocomposites are shown schematically in Fig. 12. Amorphous structures are excellent for electromagnetic wave absorption, and the presence of pores improves impedance matching, causing the electromagnetic waves to pass through several pores at different angles. This causes electromagnetic waves to propagate in different directions and paths, known as multiple reflections and scattering. These factors are ultimately associated with an in-

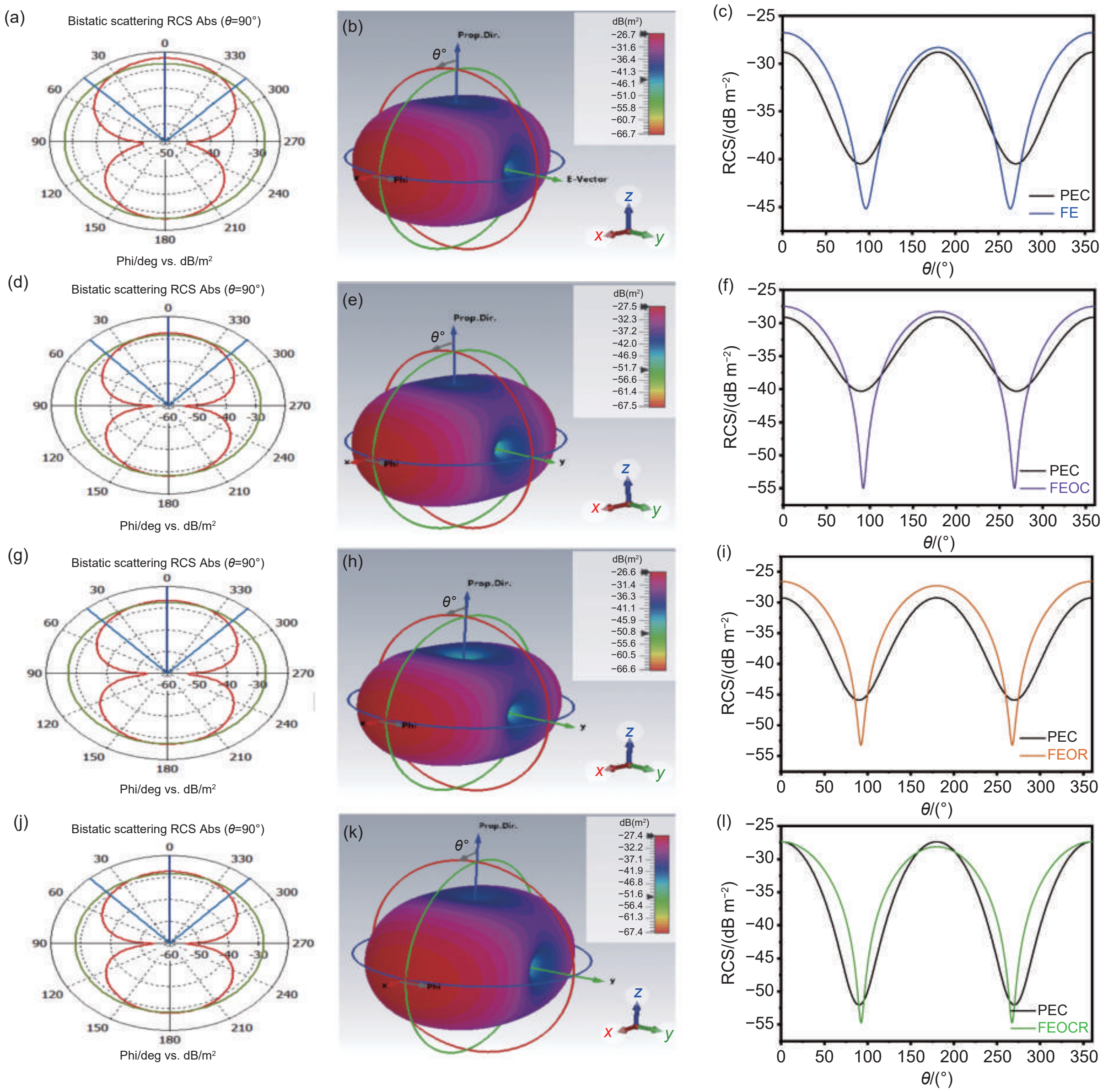

Fig. 11　2D and 3D spherical coordinate diagrams, RCS simulated curves for (a-c) FE, (d-f) FEOC, (g-i) FEOR, (j-l) FEOCR

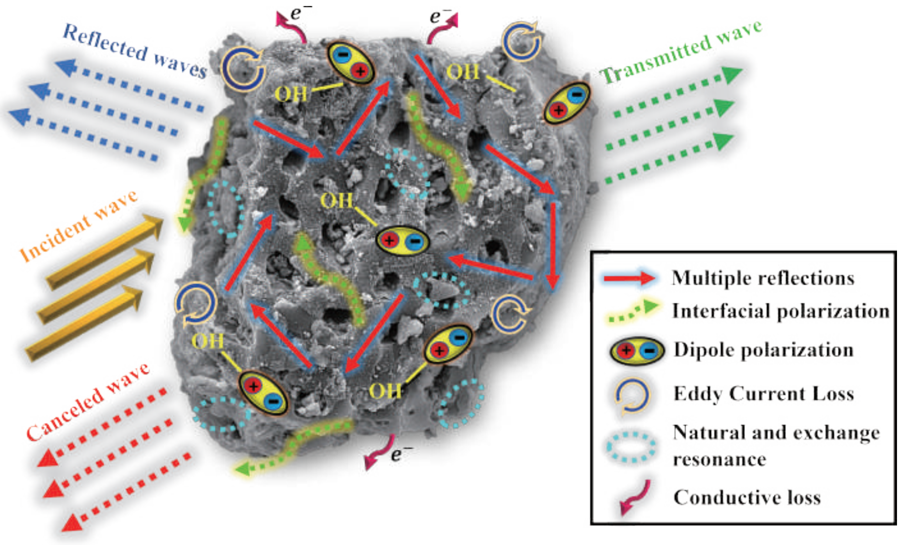

Fig. 12 Schematic illustration of the different microwave absorption mechanisms in the nanocomposites

crease in energy conversion. The reflection of waves inside the dielectric material increases the absorption of the microwaves[74]. The conjugated structure establishes conductive loss and electron hopping causes conductive networks and microcurrents[75]. Moreover, the interaction of the propagated microwaves with dielectric materials such as the carbonized structure and resin results in ionic, electron, interfacial and dipole polarization[76–79].

As mentioned, interfacial polarization (i.e., polarization caused at the interfaces of particles due to the accumulation of charge carriers) has significant effects on dielectric loss[80]. Porosity in the structure affects surface polarization. Furthermore, dipole polarization is created due to the motion of dipoles in bonded atoms with different electronegativities. Since oxygen has a high electronegativity, it causes the accumulation of electrons around the atom, creating an electron cloud. Hence, the presence of functional groups containing oxygen species in the structure of resin and activated carbon can cause dipolar polarization and absorb the energy of the incident microwaves. Defect sites in materials are also very effective in the microwave absorption process and cause the trapping of charge carriers in interactions. Therefore, the presence of points, as well as other types of defects, improves the microwave attenuation by dipole polarization. Other magnetic losses such as domain wall resonances and magnetic hysteresis are ignored. Anchoring the magnetic nanoparticles on biomaterials enhances the interfacial and dipole polarization.

Gums are obtained from plants after a natural secretion process or by extracting tissues from different exudates. These are polysaccharides in which different monosaccharide units are connected through glycosidic bonds. The gum from the apricot tree is produced in response to mechanical damage or for protection against microbial attack. The functional group distribution of gum polysaccharides in FEOR nanocomposite was studied by FT-IR analysis. The main groups OH, C—H, C—C and C—O—C are present in the gum structure. Due to the high electrical conductivity and functional groups on the surface, the FEOR nanocomposite exhibits strong ohmic losses and the ability to reduce polarization relaxation[81,82]. In the FESEM images, the gum-like plate structure is magnified. Higher electrical conductivity in the direction parallel to the transverse electromagnetic wave impingement on the plates leads to stronger attenuation capability in the vertical direction[83]. When the amount of resin is low, the weakly conducting electromagnetic wave paths in the parallel direction cannot effectively destroy the incident wave. On the contrary, the ability to absorb electromagnetic waves in the FEOR nanocomposite in the vertical direction is significantly increased due to its strong attenuation. As the proportion of tree gum is greater than carbon, the tunnel-like wave paths increasingly dissipate more and more electromagnetic waves, but magnetite nanoparticles that are more densely packed in the vertical direction lead to stronger surface reflection. Therefore, FEOR nanocomposites gradually show better absorption performance.

## 4 Conclusions

This work reports a new microwave absorber with excellent absorption performance, which was synthesized by a facile process from affordable precursors. By anchoring ferrite nanoparticles onto natural resin (FEOR), a reflection loss of –71.09 dB for a thickness of $t$ = 1 mm is achieved. Interestingly, this sample covers almost the entire X-band for $t$ = 2 mm. Additionally, the dielectric characteristics is optimized by varying the content of pyrolyzed biomass-derived material. The FEOC sample obtained from oleaster seeds, shows RL = –51.12 dB for $t$ = 1 mm, while the triphasic FEOCR nanocomposite shows RL = –29.28 dB for a thickness of 1 mm. Thus, FEOR emerges as a superior electromagnetic wave absorber due to its simple synthesis process, reasonable cost and excellent absorption bandwidth. This work sheds light on the use of biomaterials and their composites with magnetic nanoparticles to increase microwave absorption capacity.

## Acknowledgements

Bagher Aslibeiki, Rajesh Kumar Rajagopal, and Tapati Sarkar gratefully acknowledge funding from Stiftelsen Olle Engkvist Byggmästare (214-0346 and 217-0014), and the Swedish Research Council (2021-03675).

### References

[1] Cucurachi S, Tamis W L M, Vijver M G, et al. A review of the ecological effects of radiofrequency electromagnetic fields (RF-EMF)[J]. Environment International, 2013, 51: 116-140.

[2] Zhang F, Cui W, Wang B, et al. Morphology-control synthesis of polyaniline decorative porous carbon with remarkable electromagnetic wave absorption capabilities[J]. Composites Part B: Engineering, 2021, 204: 108491.

[3] Gao S, An Q, Xiao Z, et al. Significant promotion of porous architecture and magnetic $Fe_3O_4$ NPs inside honeycomb-like carbonaceous composites for enhanced microwave absorption[J]. RSC Advances, 2018, 8(34): 19011-19023.

[4] Kucheriv O I, Oliynyk V V, Zagorodnii V V, et al. Hybrid organic–inorganic perovskites as microwave radiation switches[J]. Materials Advances, 2022, 3(22): 8260-8266.

[5] Sun H, Che R, You X, et al. Cross-stacking aligned carbon-nanotube films to tune microwave absorption frequencies and increase absorption intensities[J]. Advanced Materials, 2014, 26(48): 8120-8125.

[6] Li X, Du D, Wang C, et al. In situ synthesis of hierarchical rose-like porous Fe@C with enhanced electromagnetic wave absorption[J]. Journal of Materials Chemistry C, 2018, 6(3): 558-567.

[7] Zhang Z, Cai Z, Wang Z, et al. A review on metal–organic framework-derived porous carbon-based novel microwave absorption materials[J]. Nano-Micro Letters, 2021, 13(1): 56.

[8] Jiang B, Qi C, Yang H, et al. Recent advances of carbon-based electromagnetic wave absorption materials facing the actual situations[J]. Carbon, 2023, 208: 390-409.

[9] Wu Z, Meng Z, Yao C, et al. Rice husk derived hierarchical porous carbon with lightweight and efficient microwave absorption[J]. Materials Chemistry and Physics, 2022, 275: 125246.

[10] Zhao H, Cheng Y, Lv H, et al. A novel hierarchically porous magnetic carbon derived from biomass for strong lightweight microwave absorption[J]. Carbon, 2019, 142: 245-253.

[11] Lei Y, Yao Z, Li S, et al. Broadband high-performance electromagnetic wave absorption of Co-doped NiZn ferrite/polyaniline on MXenes[J]. Ceramics International, 2020, 46(8, Part A): 10006-10015.

[12] Yan L, Zhang H, Li Y, et al. Nickel nanoparticle decorated N-doped carbon nanofibers for light weight and high-efficiency microwave absorption[J]. Dalton Transactions, 2022, 51(39): 14912-14923.

[13] Cui J, Huang L, Ma J, et al. Carbon-encapsulated core–shell structure $ZnFe_2O_4$ sphere composites coupled with excellent microwave absorption and corrosion resistance[J]. Nanoscale, 2022, 14(41): 15393-15403.

[14] Liang C, Qiu H, Song P, et al. Ultra-light MXene aerogel/wood-derived porous carbon composites with wall-like “mortar/brick” structures for electromagnetic interference shielding[J]. Science Bulletin, 2020, 65(8): 616-622.

[15] Qiu X, Wang L, Zhu H, et al. Lightweight and efficient microwave absorbing materials based on walnut shell-derived nano-porous carbon[J]. Nanoscale, 2017, 9(22): 7408-7418.

[16] Pan J, Tu W, Ma S, et al. Improvement of multiple attenuation characteristics of two-dimensional lamellar ferrocobalt@ carbon nanocomposites as excellent electromagnetic wave absorbers[J]. Dalton Transactions, 2022, 51(25): 9793-9802.

[17] B S, Patil N, Jaiswal K K, et al. Development of sustainable

alternative materials for the construction of green buildings using agricultural residues: A review[J]. Construction and Building Materials, 2023, 368: 130457.

[18] Lou Z, Han H, Zhou M, et al. Synthesis of magnetic wood with excellent and tunable electromagnetic wave-absorbing properties by a facile vacuum/pressure impregnation method[J]. ACS Sustainable Chemistry & Engineering, 2018, 6(1): 1000-1008.

[19] Khasnabis S, Hs M J, Bora P J, et al. Comparative studies on physical and chemical routes for animal waste-derived activated carbon for microwave absorption in the X-band[J]. Journal of Materials Science: Materials in Electronics, 2022, 33(7): 3425-3437.

[20] Chandran S R, T B A, Krishnan R R, et al. Conversion of aquatic weed water-hyacinth to conducting and microwave shielding material-a scientific approach[J]. Journal of Elastomers & Plastics, 2022, 54(5): 718-730.

[21] Bi Z, Yao L, Wang X, et al. Experimental and theoretical study on broadband electromagnetic wave absorption of algae-like NiO/carbon nanotubes absorbers[J]. Journal of Alloys and Compounds, 2022, 926: 166821.

[22] Hassan A, Ding W, Aslam M A, et al. Microwave absorption property of coffee waste bio-carbon modified by industrial waste $MnFe_2O_4$ particles[J]. Journal of Materials Research and Technology, 2020, 9(6): 12869-12879.

[23] Li W, Pu Y, Ying Y, et al. Magnetic properties and related mechanisms of iron-based soft magnetic composites with high thermal stability in situ composite-ferrite coating[J]. Journal of Alloys and Compounds, 2020, 829: 154533.

[24] Mingdong C, Huangzhong Y, Xiaohua J, et al. Optimization on microwave absorbing properties of carbon nanotubes and magnetic oxide composite materials[J]. Applied Surface Science, 2018, 434: 1321-1326.

[25] Xie X, Wang B, Wang Y, et al. Spinel structured $MFe_2O_4$ (M = Fe, Co, Ni, Mn, Zn) and their composites for microwave absorption: A review[J]. Chemical Engineering Journal, 2022, 428: 131160.

[26] Liu P, Yao Z, Ng V M H, et al. Facile synthesis of ultrasmall $Fe_3O_4$ nanoparticles on MXenes for high microwave absorption performance[J]. Composites Part A: Applied Science and Manufacturing, 2018, 115: 371-382.

[27] Mahmoodi M, Aslibeiki B, Peymanfar R, et al. Oleaster seed-derived activated carbon/ferrite nanocomposite for microwave absorption in the X-band range[J]. Frontiers in Materials, 2022, 9: 1088196.

[28] Li B, Tian H, Li L, et al. Graphene-assisted assembly of electrically and magnetically conductive ceramic nanofibrous aerogels enable multifunctionality[J]. Advanced Functional Materials, 2024, 34(22): 2314653.

[29] Rusly S N A, Ismail I, Matori K A, et al. Influence of different BFO filler content on microwave absorption performances in $BiFeO_3$/epoxy resin composites[J]. Ceramics International, 2020, 46(1): 737-746.

[30] Jiang B, Yang W, Wang C, et al. Lightweight porous cobalt-encapsulated nitrogen-doped carbon nanotubes for tunable, efficient and stable electromagnetic waves absorption[J]. Carbon, 2023, 202: 173-186.

[31] Zhang X, Wang Y, Shi B, et al. Strongly plasticized gelatin-based hydrogel for flexible encapsulation of complex-shaped electronic devices[J]. Iscience, 2024, 27(5):109725.

[32] Aslibeiki B, Ehsani M H, Nasirzadeh F, et al. The effect of interparticle interactions on spin glass and hyperthermia properties of $Fe_3O_4$ nanoparticles[J]. Materials Research Express, 2017, 4(7): 075051.

[33] Mahmoodi M, Aslibeiki B, Abdolalipour Sakha M, et al. Oleaster seed-derived activated carbon/ferrite nanocomposite for $Pb^{2+}$ removal from wastewater[J]. Materials Chemistry and Physics, 2023, 300: 127536.

[34] Wu H, Wu G, Wang L. Peculiar porous $\alpha$-$Fe_2O_3$, $\gamma$-$Fe_2O_3$ and $Fe_3O_4$ nanospheres: Facile synthesis and electromagnetic properties[J]. Powder Technology, 2015, 269: 443-451.

[35] Sekar M, Pandiaraj M, Bhansali S, et al. Carbon fiber based electrochemical sensor for sweat cortisol measurement[J]. Scientific Reports, 2019, 9(1): 403.

[36] Xi J, Zhou E, Liu Y, et al. Wood-based straightway channel structure for high performance microwave absorption[J]. Carbon, 2017, 124: 492-498.

[37] Wu Z, Tian K, Huang T, et al. Hierarchically porous carbons derived from biomasses with excellent microwave absorption performance[J]. ACS Appl Mater Interfaces, 2018, 10(13): 11108-11115.

[38] Wang L, Liu F, Pal A, et al. Ultra-small $Fe_3O_4$ nanoparticles encapsulated in hollow porous carbon nanocapsules for high performance supercapacitors[J]. Carbon, 2021, 179: 327-336.

[39] Kang E, Jung Y S, Cavanagh A S, et al. $Fe_3O_4$ nanoparticles confined in mesocellular carbon foam for high performance anode materials for lithium-ion batteries[J]. Advanced Functional Materials, 2011, 21(13): 2430-2438.

[40] Meng Y, Zhang Z, Hou X, et al. Flexible and ultra-thin graphene@MXene@$Fe_3O_4$ composites with excellent microwave absorption performance[J]. Ceramics International, 2024, 50(4): 6624-6633.

[41] Liu Y, Fu Y W, Liu L, et al. Low-cost carbothermal reduction preparation of monodisperse $Fe_3O_4$/C core-shell nanosheets for improved microwave absorption[J]. ACS Applied Materials & Interfaces, 2018, 10(19): 16511-16520.

[42] Govindasamy T, Mathew N K, Asapu V K, et al. Evaluating the microwave absorbing performance of polymer-free thin $Fe_3O_4$–MWCNT NCs in X-band region[J]. Surfaces and Interfaces, 2024, 44: 103716.

[43] Aghamali A, Khosravi M, Hamishehkar H, et al. Preparation of novel high performance recoverable and natural sunlight-driven nanocomposite photocatalyst of $Fe_3O_4$/C/$TiO_2$/N-CQDs[J]. Materials Science in Semiconductor Processing, 2018, 87: 142-154.

[44] Hou T, Wang B, Ma M, et al. Preparation of two-dimensional titanium carbide ($Ti_3C_2T_x$) and $NiCo_2O_4$ composites to achieve

excellent microwave absorption properties[J]. Composites Part B: Engineering, 2020, 180: 107577.

[45] Qi X, Hu Q, Cai H, et al. Heteronanostructured Co@carbon nanotubes-graphene ternary hybrids: synthesis, electromagnetic and excellent microwave absorption properties[J]. Scientific Reports, 2016, 6(1): 37972.

[46] Zheng X, Feng J, Zong Y, et al. Hydrophobic graphene nanosheets decorated by monodispersed superparamagnetic $Fe_3O_4$ nanocrystals as synergistic electromagnetic wave absorbers[J]. Journal of Materials Chemistry C, 2015, 3(17): 4452-4463.

[47] Wang Y, Gao X, Zhang W, et al. Synthesis of hierarchical CuS/RGO/PANI/$Fe_3O_4$ quaternary composite and enhanced microwave absorption performance[J]. Journal of Alloys and Compounds, 2018, 757: 372-381.

[48] Duan Y, Song L, Cui Y, et al. FeCoNiCuAl high entropy alloys microwave absorbing materials: Exploring the effects of different Cu contents and annealing temperatures on electromagnetic properties[J]. Journal of Alloys and Compounds, 2020, 848: 156491.

[49] Luo H, Gong R, Wang X, et al. $Fe_3O_4$ cladding enhanced magnetic natural resonance and microwave absorption properties of $Fe_{0.65}Co_{0.35}$ alloy flakes[J]. Journal of Alloys and Compounds, 2015, 646: 345-350.

[50] Zhang M, Ling H, Ding S, et al. Synthesis of CF@PANI hybrid nanocomposites decorated with $Fe_3O_4$ nanoparticles towards excellent lightweight microwave absorber[J]. Carbon, 2021, 174: 248-259.

[51] Ma Y, Zhou Y, Sun Y, et al. Tunable magnetic properties of $Fe_3O_4$/rGO/PANI nanocomposites for enhancing microwave absorption performance[J]. Journal of Alloys and Compounds, 2019, 796: 120-130.

[52] Wang X, Shi G, Shi F-N, et al. Synthesis of hierarchical cobalt dendrites based on nanoflake self-assembly and their microwave absorption properties[J]. RSC Advances, 2016, 6(47): 40844-40853.

[53] Fu X, Yang B, Chen W, et al. Electromagnetic wave absorption performance of $Ti_2O_3$ and vacancy enhancement effective bandwidth[J]. Journal of Materials Science & Technology, 2021, 76: 166-173.

[54] Akinay Y, Hayat F, Çolak B. Absorbing properties and structural design of PVB/$Fe_3O_4$ nanocomposite[J]. Materials Chemistry and Physics, 2019, 229: 460-466.

[55] Zheng S, Xu W, Liu J, et al. One-hour ambient-pressure-dried, scalable, stretchable MXene/polyurea aerogel enables synergistic defense against high-frequency mechanical shock and electromagnetic waves[J]. Advanced Functional Materials, 2024: 2402889.

[56] Xie J, Jiang H, Li J, et al. Improved impedance matching by multi-componential metal-hybridized rGO toward high performance of microwave absorption[J]. Nanotechnology Reviews, 2021, 10(1): 1-9.

[57] Chen L, Li Y, Zhao B, et al. Multiprincipal element $M_2FeC$ (M = Ti, V, Nb, Ta, Zr) MAX phases with synergistic effect of dielectric and magnetic loss[J]. Advanced Science, 2023, 10(10): 2206877.

[58] Qin M, Zhang L, Zhao X, et al. Lightweight Ni foam-based ultra-broadband electromagnetic wave absorber[J]. Advanced Functional Materials, 2021, 31(30): 2103436.

[59] Li Y, Sun N, Liu J, et al. Multifunctional $BiFeO_3$ composites: Absorption attenuation dominated effective electromagnetic interference shielding and electromagnetic absorption induced by multiple dielectric and magnetic relaxations[J]. Composites Science and Technology, 2018, 159: 240-250.

[60] Zhou L, Huang J, Wang H, et al. FeSiAl/ZnO-filled resin composite coatings with enhanced dielectric and microwave absorption properties[J]. Journal of Materials Science: Materials in Electronics, 2019, 30(2): 1896-1906.

[61] Wang B, Wei J, Yang Y, et al. Investigation on peak frequency of the microwave absorption for carbonyl iron/epoxy resin composite[J]. Journal of Magnetism and Magnetic Materials, 2011, 323(8): 1101-1103.

[62] F Hasany S, H Abdurahman N, R Sunarti A, et al. Magnetic iron oxide nanoparticles: chemical synthesis and applications review[J]. Current nanoscience, 2013, 9(5): 561-575.

[63] Yang W, Wang C, Jiang B, et al. Lightweight 3D interconnected porous carbon with robust cavity skeleton derived from petroleum pitch for effective multi-band electromagnetic wave absorption[J]. Carbon, 2022, 200: 390-400.

[64] Liu X, Guo H, Xie Q, et al. Enhanced microwave absorption properties in GHz range of $Fe_3O_4$/C composite materials[J]. Journal of Alloys and Compounds, 2015, 649: 537-543.

[65] He Y, Chen Q, Yang S, et al. Micro-crack behavior of carbon fiber reinforced $Fe_3O_4$/graphene oxide modified epoxy composites for cryogenic application[J]. Composites Part A: Applied Science and Manufacturing, 2018, 108: 12-22.

[66] Wang R, Yang E, Qi X, et al. Constructing and optimizing core@shell structure CNTs@$MoS_2$ nanocomposites as outstanding microwave absorbers[J]. Applied Surface Science, 2020, 516: 146159.

[67] Li Y, Wang G, Gong A, et al. High-performance ferroelectric electromagnetic attenuation materials with multiple polar units based on nanodomain engineering[J]. Small, 2022, 18(12): 2106302.

[68] Guan H, Wang H, Zhang Y, et al. Microwave absorption performance of $Ni(OH)_2$ decorating biomass carbon composites from Jackfruit peel[J]. Applied Surface Science, 2018, 447: 261-268.

[69] Wang Y, Yao L, Zheng Q, et al. Graphene-wrapped multiloculated nickel ferrite: A highly efficient electromagnetic attenuation material for microwave absorbing and green shielding[J]. Nano Research, 2022, 15(7): 6751-6760.

[70] Wang L, Yu X, Li X, et al. MOF-derived yolk-shell Ni@C@ ZnO Schottky contact structure for enhanced microwave absorption[J]. Chemical Engineering Journal, 2020, 383: 123099.

[71] Chen W, Peng K, Wang J, et al. Enhanced microwave absorption

properties of nickel-coated carbon fiber/glass fiber hybrid epoxy composites-towards an industrial reality[J]. Materials Research Express, 2020, 6(12): 126324.

[72] Zhan B, Qu Y, Qi X, et al. Mixed-dimensional assembly strategy to construct reduced graphene oxide/carbon foams heterostructures for microwave absorption, anti-corrosion and thermal insulation[J]. Nano-Micro Letters, 2024, 16(1): 221.

[73] Cheng X-D, Song W-L, Chen M, et al. Metallic origami metastructures for high-temperature low electromagnetic reflectivity[J]. Journal of Materials Science, 2019, 54(8): 6425-6433.

[74] Pan F, Shi Y, Yang Y, et al. Porifera-inspired lightweight, thin, wrinkle-resistance, and multifunctional MXene foam[J]. Advanced Materials, 2024, 36(14): 2311135.

[75] Che R C, Peng L M, Duan X F, et al. Microwave absorption enhancement and complex permittivity and permeability of Fe encapsulated within carbon nanotubes[J]. Advanced Materials, 2004, 16(5): 401-405.

[76] Thirumurugan A, Ramadoss A, Dhanabalan S S, et al. MXene/ferrite magnetic nanocomposites for electrochemical supercapacitor applications[J]. Micromachines, 2022, 13(10): 1792.

[77] Li Z, Lin H, Ding S, et al. Synthesis and enhanced electromagnetic wave absorption performances of $Fe_3O_4$@C decorated walnut shell-derived porous carbon[J]. Carbon, 2020, 167: 148-159.

[78] Cui K, Cheng Y, Dai J, et al. Synthesis, characterization and microwave absorption properties of $La_{0.6}Sr_{0.4}MnO_3$/polyaniline composite[J]. Materials Chemistry and Physics, 2013, 138(2-3): 810-816.

[79] Jiang B, Yang W, Bai H, et al. Multiscale structure and interface engineering of Fe/$Fe_3C$ in situ encapsulated in nitrogen-doped carbon for stable and efficient multi-band electromagnetic wave absorption[J]. Journal of Materials Science & Technology, 2023, 158: 9-20.

[80] Qiao J, Song Q, Xuan L, et al. Dual cross-linked magnetic MXene aerogel with high strength and durability enables multifunctionality[J]. Advanced Functional Materials, 2024: 2401687.

[81] Qiao J, Song Q, Zhang X, et al. Enhancing interface connectivity for multifunctional magnetic carbon aerogels: An in situ growth strategy of metal-organic frameworks on cellulose nanofibrils[J]. Advanced Science, 2024, 11(19): 2400403.

[82] Yang W, Jiang B, Che S, et al. Research progress on carbon-based materials for electromagnetic wave absorption and the related mechanisms[J]. New Carbon Materials, 2021, 36(6): 1016-1030.

[83] Zhang X, Tian X, Wu N, et al. Metal-organic frameworks with fine-tuned interlayer spacing for microwave absorption[J]. Science Advances, 2024, 10(11): eadl6498.

[84] Wu F, Yang K, Li Q, et al. Biomass-derived 3D magnetic porous carbon fibers with a helical/chiral structure toward superior microwave absorption[J]. Carbon, 2021, 173: 918-931.

[85] Zhao H, Jin C, Lu P, et al. Anchoring well-dispersed magnetic nanoparticles on biomass-derived 2D porous carbon nanosheets for lightweight and efficient microwave absorption[J]. Composites Part A: Applied Science and Manufacturing, 2022, 154: 106773.

[86] Singh S K, Prakash H, Akhtar M, et al. Lightweight and high-performance microwave absorbing heteroatom-doped carbon derived from chicken feather fibers[J]. ACS Sustainable Chemistry & Engineering, 2018, 6(4): 5381-5393.

[87] Huang L, Li J, Wang Z, et al. Microwave absorption enhancement of porous C@$CoFe_2O_4$ nanocomposites derived from eggshell membrane[J]. Carbon, 2019, 143: 507-516.

[88] Gou G, Meng F, Wang H, et al. Wheat straw-derived magnetic carbon foams: In-situ preparation and tunable high-performance microwave absorption[J]. Nano Research, 2019, 12: 1423-1429.

[89] MT Uddin, Rukanuzzaman, MMR Khan, et al. Jackfruit (Artocarpus heterophyllus) leaf powder: An effective adsorbent for removal of methylene blue from aqueous solutions[J]. Indian Journal of Chemical Technology, 2009, 16(2): 142-149.

[90] Zhao H, Seow J Z Y, Cheng Y, et al. Green synthesis of hierarchically porous carbons with tunable dielectric response for microwave absorption[J]. Ceramics International, 2020, 46(10): 15447-15455.

[91] Zhao D, Zhao Q, Feng L, et al. Honey-comb carbon nanostructure derived from peach gum to yield high microwave absorption[J]. Journal of Materials Science: Materials in Electronics, 2021, 32: 25829-25839.

[92] Kang H, Luo S, Du H, et al. Bio-based eucommia ulmoides gum composites with high electromagnetic interference shielding performance[J]. Polymers, 2022, 14(5): 970.